The Astrophysical Journal, 982:143 (10pp), 2025 April 1 https://doi.org/10.3847/1538-4357/adbbd0

When is a Bulge Not a Bulge? Revealing the Satellite Nature of NGC 5474's Bulge

Ray Garner, III[1,2], J. Christopher Mihos[3], and F. Fabián Rosales-Ortega[4]
[1] Department of Physics and Astronomy, Texas A&M University, 578 University Dr., College Station, TX 77843, USA; ray.three.garner@gmail.com
[2] George P. and Cynthia W. Mitchell Institute for Fundamental Physics & Astronomy, Texas A&M University, 578 University Dr., College Station, TX 77843, USA
[3] Department of Astronomy, Case Western Reserve University, 10900 Euclid Ave., Cleveland, OH 44106, USA
[4] Instituto Nacional de Astrofísica, Óptica y Electrónica, Luis Enrique Error 1, 72840 Tonantzintla, Mexico
Received 2024 December 17; revised 2025 February 20; accepted 2025 February 28; published 2025 March 26

Abstract

A satellite galaxy of the nearby spiral M101, NGC 5474 has a prominent bulge offset from the kinematic center of the underlying star-forming disk that has gained attention in recent years. Recent studies have proposed that this putative offset bulge is not a classical bulge within the plane of the disk but instead a dwarf companion galaxy along the line of sight. Using integral field spectroscopy data taken as part of the PPak IFS Nearby Galaxies Survey (PINGS), we perform the first analysis of the stellar and gas kinematics of this putative bulge (PB) and portions of the disk. We find a radial velocity offset of $\sim$24 km s^{-1} between the emission lines produced by the disk H II regions and the absorption lines produced by the PB stellar component. We interpret this velocity offset as evidence that the PB and disk are two separate objects, the former orbiting around the latter, supporting simulations and observations of this peculiar system. We attempt to place this external companion into the context of the M101 Group and the M101-NGC 5474 interaction.

Unified Astronomy Thesaurus concepts: Galaxy interactions (600); Galaxy evolution (594); Galaxy kinematics (602); Galaxy spectroscopy (2171)

1. Introduction

Located within the M101 Group at a distance of 6.9 Mpc (see T. Matheson et al. 2012 and references therein) lies NGC 5474, a peculiar star-forming galaxy. In this sparsely populated group, NGC 5474 is the largest and brightest ($R_{25} = 2\farcm4$, $M_B \simeq -17.9$; G. de Vaucouleurs et al. 1991) satellite galaxy of M101 (NGC 5457), which is itself a peculiar galaxy. NGC 5474 is also relatively close to M101, with a projected angular separation of 44′, corresponding to a physical separation of 88 kpc. This relatively close separation and the lack of other massive galaxies in the M101 Group have led many authors to propose that a recent interaction between M101 and NGC 5474 is responsible for producing the peculiarities seen in M101 (e.g., J. S. Beale & R. D. Davies 1969; W. H. Waller et al. 1997; J. C. Mihos et al. 2012, 2013, 2018; J.-L. Xu et al. 2021; R. Garner et al. 2022, 2024; S. T. Linden & J. C. Mihos 2022).

However, just like M101, NGC 5474 is home to numerous asymmetries and oddities remarked upon over the years (D. A. Kornreich et al. 1998). Early observations focused on its H I disk and found a smoothly varying disk in the central region out to 5 kpc, beyond which lie distortions with a change in position angle by as much as $\simeq$50° (B. K. Rownd et al. 1994). The H I disk of NGC 5474 is also connected to the southwestern edge of M101 via a bridge of intermediate-velocity H I gas (W. K. Huchtmeier & A. Witzel 1979; J. M. van der Hulst & W. K. Huchtmeier 1979), interpreted as tidal debris from the M101–NGC 5474 interaction (J. C. Mihos et al. 2012). However, researchers have not found any optical debris down to extremely low surface brightnesses, $\mu_V \sim 28$ (J. C. Mihos et al. 2013; R. Garner et al. 2021).

Optically, NGC 5474 appears as a typical dwarf spiral galaxy with loose spiral arms, circular outer isophotes (J. C. Mihos et al. 2013), and numerous sites of star formation, including an extended UV disk (D. A. Thilker et al. 2007). The left panel of Figure 1 illustrates the exception: an optical bulge at the northern edge of a nearly face-on stellar disk. The bulge does not appear strikingly offset with respect to the overall spiral pattern of the disk but instead shows a 1 kpc offset north from the kinematic center of NGC 5474's H I and Hα disks (B. K. Rownd et al. 1994; D. A. Kornreich et al. 2000; B. Epinat et al. 2008).

Historically, the offset bulge has been gathered together with the H I distortions and bridge as being caused by the interaction NGC 5474 had with M101 $\sim$ 300 Myr ago (J. C. Mihos et al. 2013, 2018; S. T. Linden & J. C. Mihos 2022). However, recent work has called the nature of this bulge into question. M. Bellazzini et al. (2020) renewed interest in NGC 5474, finding that the putative bulge (PB; adopting the nomenclature of R. Pascale et al. 2021) has many structural properties similar to dwarf galaxies, especially M110 (NGC 205), a dwarf elliptical satellite galaxy of M31. They proposed that NGC 5474 also bears the signs of a recent interaction with a dwarf companion and pointed to the PB as the culprit. R. Pascale et al. (2021) used *N*-body hydrodynamical simulations to investigate this possibility and found that it is highly unlikely that the PB resides in the plane of the galaxy. Suppose, instead, the PB was an early-type satellite galaxy on a polar orbit around NGC 5474. In that case, simple projection effects can produce the apparent offset, and the interaction between the two bodies explains the warped H I disk. Most recently, G. Bortolini et al. (2024) investigated the star formation histories of the PB, disk, and an overdensity of stars to the southwest and found a synchronized burst of activity around 10–35 Myr ago, which they interpret as a signature of a more recent interaction between the disk and PB.

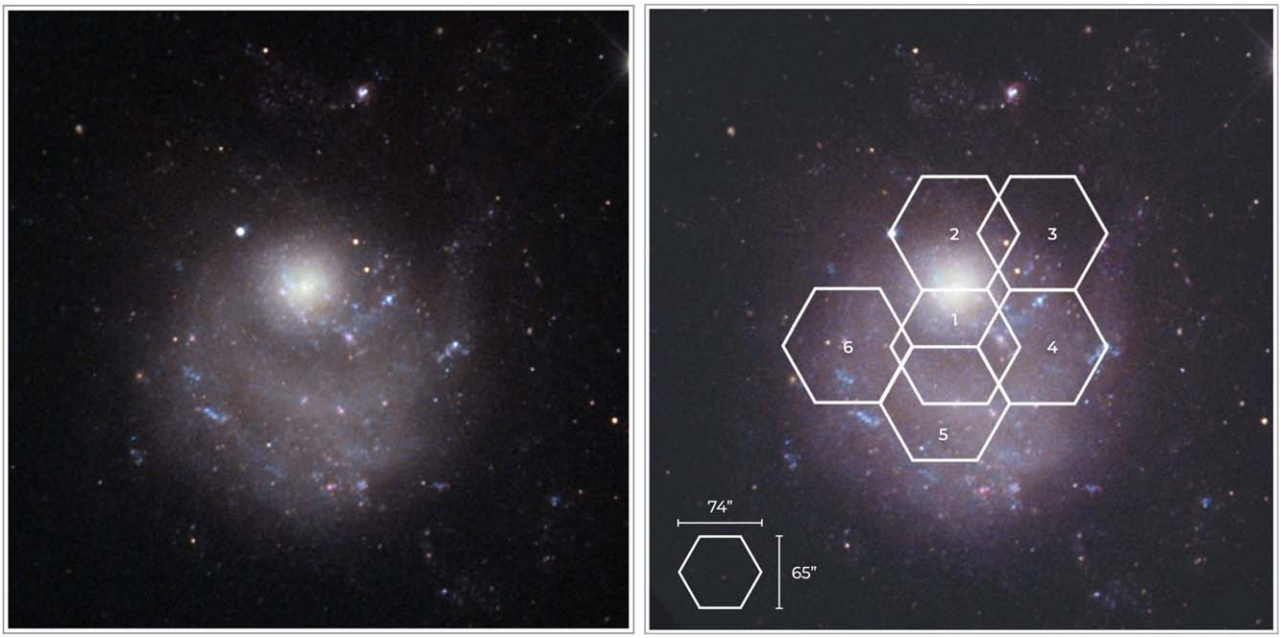

Figure 1. An RGB color image of NGC 5474 with (right) and without (left) overlaid PPak pointings. Both images measure $6' \times 6'$. North is up and east is to the left. Credits: KPNO/NOIRLab/NSF/AURA/Adam Block.

Despite the growing body of evidence that suggests the disk of NGC 5474 and the PB are two separate objects, no conclusive evidence in the form of a radial line-of-sight velocity difference or offset has been shown. Unfortunately, all of the available stellar velocity fields are based on emission lines that trace the star-forming disk (L. C. Ho et al. 1995; B. Epinat et al. 2008; J. Moustakas et al. 2010), while the PB is dominated by old- and intermediate-age stars with kinematics best traced by absorption line spectra. Thus, we need spatially resolved integral field spectroscopy (IFS) data sets that provide both emission line and absorption line measurements. This type of data has been used in the past to distinguish between relaxed virialized systems and merger events (e.g., H. Flores et al. 2006; K. L. Shapiro et al. 2008; E. Bellocchi et al. 2012; E. Bellocchi et al. 2013; S. Torres-Flores et al. 2014; S. Oh et al. 2022), including merger stages (J. K. Barrera-Ballesteros et al. 2015), and measuring a radial velocity offset would be relatively simple to perform.

M. Bellazzini et al. (2020) proposed and attempted exactly this methodology. Due to the limitations of their data, they could only conclude that the radial velocity difference between the emission and absorption within the PB is $\lesssim 50\,\mathrm{km\,s^{-1}}$. This small velocity offset rules out a chance superposition of kinematically unrelated systems, but the critical question of the nature of the PB was left unanswered. In this paper, we attempt to conclusively measure a velocity offset between the disk and PB of NGC 5474 using IFS data acquired as part of the PPak IFS Nearby Galaxies Survey (PINGS). Owing to the generous wavelength range and large field of view (FOV), we can extract two-dimensional (2D) velocity maps for both the stellar and ionized gas components across much of the galaxy. These maps' velocity differences should answer the outstanding question of NGC 5474's peculiar PB.

2. Observations and Data Reduction

The spectroscopic observations of NGC 5474 are part of PINGS (F. F. Rosales-Ortega et al. 2010), a project aimed at constructing 2D spectroscopic mosaics for a sample of nearby spiral galaxies. The PINGS observations were conducted using the 3.5 m telescope at the Calar Alto Observatory with the Potsdam Multi-Aperture Spectrophotometer (M. M. Roth et al. 2005) in PPak mode (M. A. W. Verheijen et al. 2004; A. Kelz et al. 2006). This mode employs a retrofitted bare bundle of 331 optical fibers, sampling the target with a spatial resolution of $2\farcs7$ per fiber over a hexagonal area with a $74'' \times 65''$ footprint and a 65% filling factor. The sky background is sampled by 36 additional fibers arranged in six mini-IFU bundles of 6 fibers each, distributed in a circular pattern at $\sim 90''$ from the center and at the edges of the central hexagon. Additionally, 15 fibers are illuminated by internal lamps for calibration purposes. The instrument was configured with the V300 grating, covering a wavelength range of 3700–7100 Å with a spectral resolution of $\sim$10 Å FWHM, corresponding to a velocity $\sim 460\,\mathrm{km\,s^{-1}}$ for Hα. While this FWHM velocity resolution is rather high, our subsequent analysis using PPXF (Section 3) provides much higher velocity accuracy on the fitted spectra (see also M. Cappellari 2017, Section 4).

Different observing strategies were employed depending on the size of the PINGS galaxies, which ranged from $\sim 1'$ to $10'$ in diameter. By construction, the initial exposure was positioned at a predefined geometrical position, which, contingent on the galaxy's morphology or the selected mosaicing pattern, may or may not coincide with the galaxy's bright bulge. Subsequent pointings generally followed a hexagonal pattern, aligning the mosaic pointings with the shape of the PPak science bundle. Each pointing center was radially offset by $60''$ from the previous one. Due to the shape of the PPak bundle and the design of the mosaics, 11 spectra at the edge of each hexagon overlapped with the same number of spectra from the preceding pointing. This strategy was chosen to maximize the covered area while ensuring sufficient overlap to align the exposures taken under varying atmospheric conditions and/or at different epochs.

In the case of NGC 5474, the original strategy was to observe the galaxy with a standard mosaic configuration comprising one central position and one concentric ring. This configuration would cover the optical area of the galaxy ($\sim$4.′8 $\times$ 4.′3). However, due to the distorted morphology of NGC 5474, the position of the central pointing was selected to ensure that the entire mosaic would encompass the optical area of the galaxy symmetrically. This configuration implied a 30″ offset in declination (toward the south) of the central position with respect to the bright pseudobulge of the galaxy. The initial two positions were observed in 2008 June, employing this scheme. However, positions 3 to 6 were observed in service mode in 2008 August. The previous central coordinates of position 1 were not properly recovered, and the bright pseudobulge was chosen as the reference for the mosaicing during this run, resulting in the odd mosaic scheme depicted in the right panel of Figure 1. The alignment of the pointings was refined during the final data reduction using broadband images (see below).

All positions were observed in dithering mode, taking three dithered exposures per position. Positions 1 and 2 were repeated during a third run in 2009 April due to quality issues in the initial observations. For position 6, the dithering was incomplete due to the low altitude of the object. The acquisition time per PPak field in dithering mode was 2 $\times$ 600 s per dithering frame (i.e., 60 minutes of exposure per position). The average seeing was 1.″3 with a maximum of 1.″5 over the three observing runs (below the fiber size). The total exposure time for the PINGS observations of NGC 5474 amounts to 6 hr. These exposure times provided spectroscopy with S/N $\geqslant$ 20 in the continuum and S/N $\geqslant$ 50 in the Hα emission line for the brightest H II regions. In total, 5958 individual spectra were obtained for this galaxy.

The reduction of the PINGS observations for NGC 5474 followed the standard steps for fiber-based IFS. Prereduction processing was performed using standard IRAF[5] packages, while the main reduction was performed using the R3D software for fiber-fed and IFS data (S. F. Sánchez 2006) in combination with the E3D and PINGSOFT IFS visualization and manipulation software (S. F. Sánchez 2004; F. F. Rosales-Ortega 2011). This process produces distortion- and transmission-corrected, sky-subtracted, and wavelength- and relative flux-calibrated spectra. An additional spectrophotometric calibration correction was applied by comparing the IFS data with *B*, *V*, *R*, and Hα imaging photometry from the SINGS legacy survey (R. C. Kennicutt et al. 2003). The estimated spectrophotometric accuracy of the IFS mosaic is approximately 0.2 mag. During this renormalization process, the relative astrometric accuracy between the pointings of the IFS mosaic was improved to a $\sim$0.″3 level based on the rms of the centroid differences of foreground stars. Finally, the fiber-based IFS data for NGC 5474 were spatially resampled into a data cube with a regular grid of 1″ spaxel^{-1} using a flux-conserving, natural neighbor, nonlinear interpolation method, as described in S. F. Sánchez et al. (2012), developed for the CALIFA survey. A detailed explanation of the observing strategy and data reduction can be found in F. F. Rosales-Ortega et al. (2010).

[5] IRAF is distributed by the National Optical Astronomy Observatories, which are operated by the Association of Universities for Research in Astronomy, Inc., under cooperative agreement with the National Science Foundation.

During the analysis detailed in the next section, we noticed a systematic offset in the sky coordinates of the final data cube. Using the centroids of two bright stars from the Two Micron All Sky Survey All-Sky Catalog of Point Sources (M. F. Skrutskie et al. 2006) that are also in the PPak FOV, we measured the offset and found that the PPak coordinates are shifted 5″ to the northwest. In the remainder of this paper, we have either corrected any reported coordinates for this offset or used relative coordinates.

3. Data Analysis

In order to determine the nature of the PB of NGC 5474, we relied on the distinct stellar populations that make up the disk and PB and their resulting spectra. Old- and intermediate-age stars primarily produce the light of the offset PB, while young stellar populations and gaseous H II regions contribute to the disk light (M. Bellazzini et al. 2020; G. Bortolini et al. 2024). Thus, where the PB dominates the light profile, the absorption lines present in the stellar continuum should trace its kinematics. In contrast, emission lines produced by the H II regions trace the disk kinematics. If the PB is kinematically separate from the disk, the two spectral components should be offset according to their radial velocities. This is the technique proposed (and attempted) by M. Bellazzini et al. (2020).

We used two methods to measure the radial velocity offset between the disk and PB. The first method sums the total light within a series of circular apertures centered on the PB to measure the radial velocities of the absorption and emission lines. This technique has the benefit of increasing the signal-to-noise ratio (S/N) of the data. The second method utilized our entire FOV to produce 2D spatially resolved velocity maps. This method necessarily reduces the S/N but puts the PB into dynamical context with the rest of the disk. However, both techniques give the same answer: a radial velocity offset of $\simeq$24 km s^{-1} between the disk and PB. We detail both methods in the following subsections.

Since both methods rely on the Python version of the penalized pixel-fitting code PPXF (v9.1.1; M. Cappellari & E. Emsellem 2004; M. Cappellari 2017, 2023) to fit the spectra and extract radial velocities, we detail our setup here. The PPXF code requires the user to select a base set of stellar population templates to construct the final model. We adopted the G. Bruzual & S. Charlot (2003) high-resolution model templates for this analysis. These models adopt an E. E. Salpeter (1955) initial mass function and the Padova isochrones (P. Marigo et al. 2008). We broaden these templates to match the spectral resolution of the PINGS data using the `log_rebin` code provided with the PPXF package. During the fitting process, we use tenth-order additive polynomials and no multiplicative polynomials. In the following subsections, we remark on how we apply PPXF specifically in each method.

3.1. Circular Apertures on the Putative Bulge

This method extracts spectra summed over circular apertures centered at the location of the PB. The radius of the aperture is a trade-off between disk contamination and the total S/N. Smaller apertures minimize contamination from the disk stellar light but yield a lower S/N, while bigger apertures maximize the total light and S/N but add more disk stellar light. Therefore, we extracted the total spectrum in four apertures with radii varying from 5″ to 20″ in 5″ increments; beyond 20″

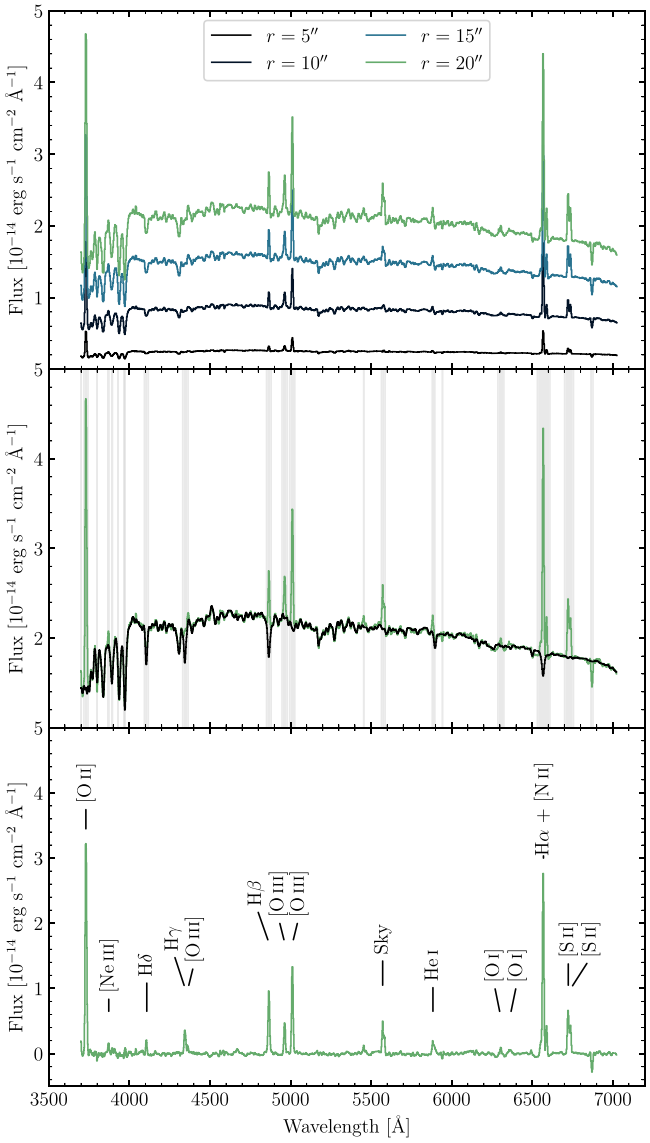

Figure 2. The spectra in circular apertures centered on the bulge of NGC 5474. The top panel shows the spectra for the four apertures used with their radii indicated in the legend. The middle panel shows an example of the PPXF fit to the stellar continuum overlaid in black for the 20″ spectrum. The light-gray bands correspond to the spectral regions masked during the stellar continuum fitting. The bottom panel shows the residual after subtracting the model from the original spectrum; the detected emission lines are labeled.

the data quality decreases. The top panel of Figure 2 shows the resulting spectra. Each aperture contains absorption lines from the PB and emission lines from H II regions in the disk.

To understand the origin of the changing properties with aperture size, we need to quantify the fraction of light contributed by the PB within our apertures. We adapted the method from M. Bellazzini et al. (2020), using the *V* band image from J. C. Mihos et al. (2013) to derive the radial flux profile of the PB and the surrounding disk. We used a series of circular apertures extending out to 145″, where within each aperture we determined the median flux value and fitted the resulting profile. To estimate the contribution of the underlying disk, we calculated the average flux from the radial light profile. We calculated the radial fraction of light attributed to the PB using these values. Table 1 lists the fraction of the PB light, $f_{\rm PB}$, in each circular aperture. As expected, the PB dominates the innermost 5″ aperture with $f_{\rm PB} = 88.1\%$, while the fraction decreases to $f_{\rm PB} = 77.0\%$ in the 20″ aperture.

We apply PPXF twice to each spectrum. The first pass is to fit only the stellar velocity and velocity dispersion. During this pass, we mask the emission lines and outliers using the method outlined in Section 6.5 of M. Cappellari (2023). In order to estimate the uncertainties on the resulting parameters, we used the wild bootstrapping method of R. Davidson & E. Flachaire (2008) and applied it 500 times. In short, this is the same as standard residual bootstrapping, but the residual for each data point is randomly multiplied by +1 or −1 with a probability of 0.5 before resampling in order to account for heteroskedasticity in the data. The middle panel of Figure 2 shows an example fit to the stellar continuum of the 20″ aperture spectrum. We automatically mask the regions in the light-gray bands during the fitting process.

After fitting for the stellar continuum and its kinematics, the second pass of PPXF fixes constant the stellar continuum model and fits for the emission lines. We take the median stellar kinematics as the fixed values. Again, we apply the wild bootstrapping method 500 times to estimate the uncertainties in the gas kinematics. The bottom panel of Figure 2 shows an example of the emission line spectrum in the 20″ aperture after subtracting the best stellar continuum model from the data. Various emission lines are labeled.

Histograms showing the bootstrapped values of the stellar and gas kinematics and both light-weighted and mass-weighted ages and metallicities are shown in Figure 3. The median values are reported in Table 1. In addition to the median values, we quantify the spread of these histograms with the standard deviation, reported in Table 1 as the uncertainties on each measurement. We stress that these are not the uncertainties on any individual measurement of a particular property. Previous work using simulated spectra at a resolution comparable to the PINGS data has explored the true uncertainties on a single fit (E. Mármol-Queraltó et al. 2011; S. F. Sánchez et al. 2016). For instance, E. Mármol-Queraltó et al. (2011) found a velocity recovery error of $\lesssim$5%. Thus, an error of $\simeq$10 km s^{-1} on any individual fit of the stellar velocity is likely present. These individual measurement uncertainties do not impact our broad conclusions below since relative velocity differences are typically better constrained than absolute velocity measurements as the overall instrumental systematic uncertainties tend to cancel out. We refer the interested reader to the aforementioned papers for more information.

The stellar velocity is approximately constant at 230 km s^{-1} after an initial decrease of 5 km s^{-1} from 5″ to 10″ apertures. The higher stellar velocity in the 5″ aperture is statistically consistent with the velocities measured in the larger apertures. The gas velocities remain constant at 255 km s^{-1}. Since we measure these from H II regions located in the disk, we take this velocity as the radial velocity of the disk.

Meanwhile, the stellar velocity dispersion increases as the aperture size increases. While PPXF does automatically remove the instrumental dispersion, there are still contributions from the disk as well as the line-of-sight velocity difference between the PB and disk. Given the PB light fractions in Table 1, the velocity dispersion measured in the 5″ aperture is likely most characteristic of the true velocity dispersion of the PB, although it is likely an upper limit (see also the discussion in M. Cappellari 2017).

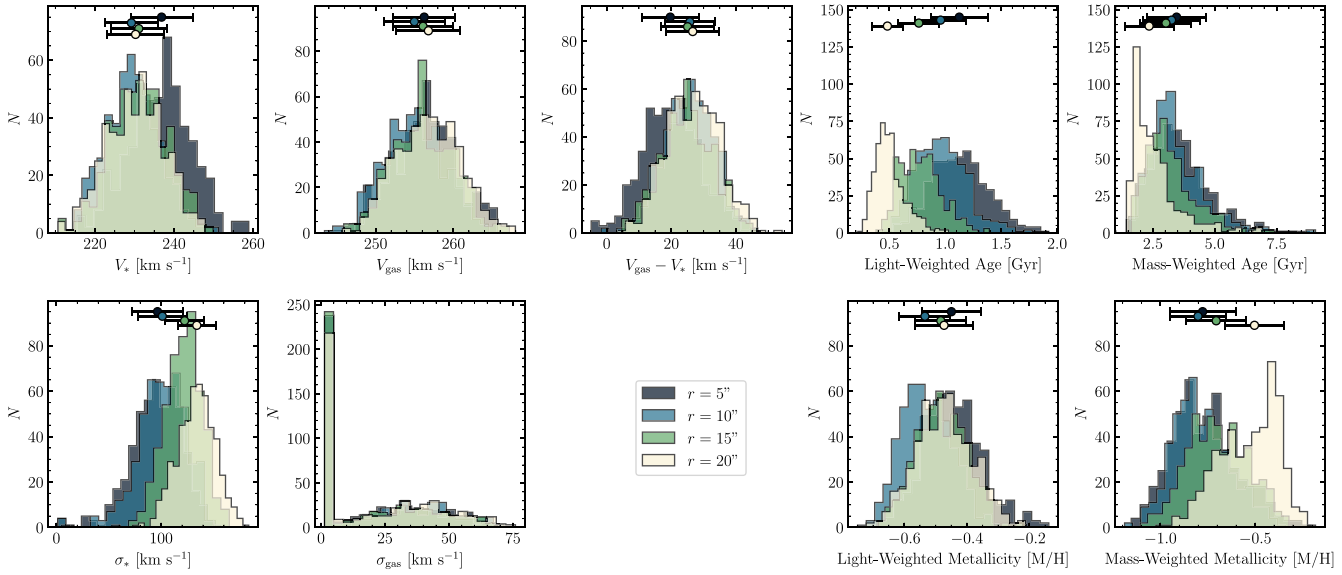

Figure 3. The histograms of our bootstrapping procedure for each aperture size. From top to bottom, left to right: stellar velocity, stellar velocity dispersion, gas velocity, gas velocity dispersion, $V_{gas} - V_*$ velocity difference, light-weighted age and metallicity, and mass-weighted age and metallicity. In each panel, the different aperture sizes are indicated by different colors; see the legend in the bottom–center. The points with error bars at the top of each panel indicate the median and standard deviation of the histograms. Those values are reported in Table 1. For the gas velocity dispersion, the dispersions often failed to converge, leading to the unphysical peak at small dispersion values. For this reason, we do not calculate the mean and standard deviation for the gas velocity dispersion.

Table 1
Median Properties of the Bootstrapped Apertures

Property	5″	10″	15″	20″
Bulge Light Fraction, f_{PB}	88.1%	85.3%	81.6%	77.0%
Stellar Velocity, V_* [km s^{-1}]	236.9 ± 7.9	229.2 ± 6.7	231.1 ± 7.1	230.3 ± 7.3
Stellar Velocity Dispersion, σ_* [km s^{-1}]	96.6 ± 24.6	101.2 ± 23.6	122.4 ± 18.4	134.1 ± 18.0
Gas Velocity, V_{gas} [km s^{-1}]	256.2 ± 4.0	255.0 ± 3.9	256.1 ± 3.9	256.8 ± 4.1
Light-weighted Age [Gyr]	1.1 ± 0.3	1.0 ± 0.2	0.8 ± 0.2	0.5 ± 0.1
Mass-weighted Age [Gyr]	3.5 ± 1.2	3.3 ± 1.1	3.0 ± 1.0	2.3 ± 1.0
Light-weighted Metallicity [M/H]	−0.45 ± 0.09	−0.53 ± 0.08	−0.48 ± 0.08	−0.47 ± 0.09
Mass-weighted Metallicity [M/H]	−0.78 ± 0.17	−0.80 ± 0.15	−0.71 ± 0.16	−0.50 ± 0.16
$V_{gas} - V_*$ [km s^{-1}]	19.7 ± 8.8	25.7 ± 7.7	25.0 ± 8.1	26.6 ± 8.2

Note. The median and standard deviation of the bootstrapped values of the stellar population histograms in Figure 3. The last row reports the velocity difference between the gas and stellar velocities by calculating the median and standard deviation of $V_{gas} - V_*$.

In the case of the gas velocity dispersion, there are a large number of bootstrapped solutions that give a dispersion of $\sim$1 km s^{-1}. This is likely the result of a "failure mode" in PPXF where the gas velocity dispersion is unresolved in the spectra. Given the large FWHM of the V300 grating ($\sim$10 Å or $\sim$460 km s^{-1} at Hα), larger than the internal velocities of H II regions (e.g., J. Garcìa-Vázquez et al. 2023), this is not surprising. Therefore, we show the histograms in Figure 3 but do not report any median values. We checked whether these "failed" solutions had any effect on the gas velocities, and they did not.

Both the light- and mass-weighted ages and metallicities show variations with aperture size. As the aperture grows, both ages become younger, while the light-weighted metallicities remain constant at ~-0.5 and the mass-weighted metallicities become more metal-rich although still subsolar. The constant light-weighted metallicities are understood to be dominated by the PB since that dominates the light profile at all aperture sizes (Table 1). Meanwhile, the mass-weighted metallicities change with aperture size because at large apertures, the disk contributes more mass, leading to younger ages and more metal-rich populations. Interestingly, the secondary peak in stellar metallicity at [M/H] ~ -0.4 is remarkably similar to the gas-phase metallicity measured in H II regions in this galaxy by J. Moustakas et al. (2010).

Finally, we can measure the velocity difference between the gas and stellar components. The median and standard deviations of $V_{gas} - V_*$ in each aperture are reported in Table 1. Averaging over the four apertures, we find a velocity difference of $\simeq$24 km s^{-1} between the stellar absorption lines and the gas emission lines. We have also checked whether $V_{gas} - V_*$ changes if we measure the differences in the individual median values and propagate the uncertainties. This is identical within the uncertainties, as expected for an approximately Gaussian distribution (Figure 3).

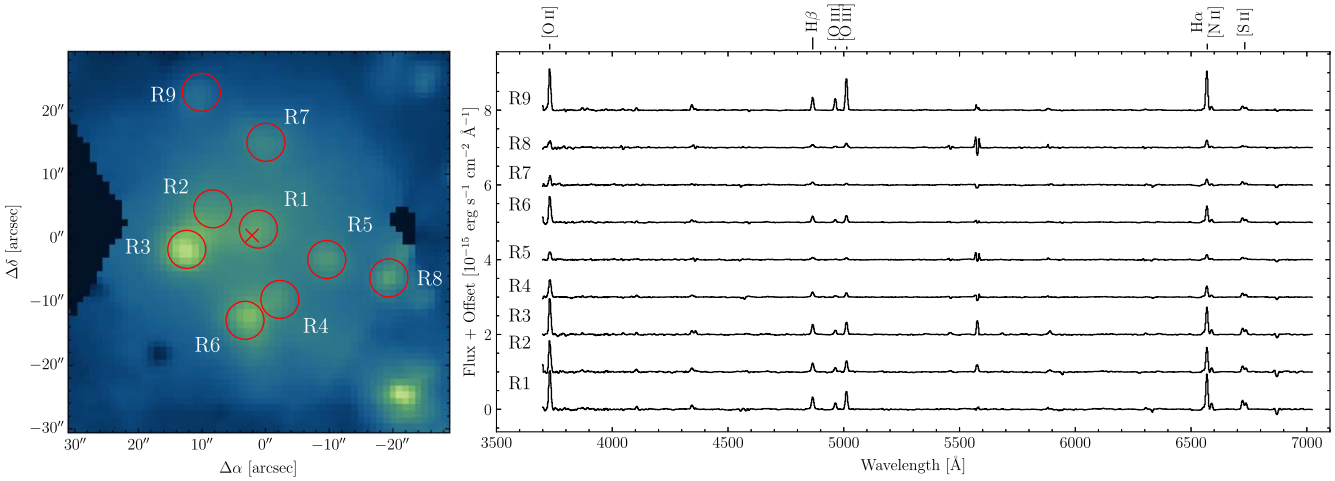

Figure 4. Nine H II regions in the region of the PB. The left panel shows a narrowband image selected from the data cube centered on the Hα emission line with a width of 22 Å. Circled in red and labeled are the nine selected H II regions. The circles measure 3″ in radius. The red cross marks the center of NGC 5474. The right panel shows the spectra of the H II regions. The strong lines used in the fitting process are labeled at the top of the panel.

As a consistency check on the gas velocities measured by PPXF, we also measured the individual strong lines' wavelengths in the disk's H II regions. Figure 4 shows the locations and spectra in 3″ apertures of nine H II regions in the PB region of NGC 5474. After subtracting the stellar continuum using PPXF as described above, we fit a model consisting of nine Gaussians simultaneously to the strongest emission lines: [O II] λ3727, Hβ, [O III]$\lambda\lambda$4959,5007, [N II]$\lambda\lambda$6548,6583, Hα, and [S II]$\lambda\lambda$6717,6731. In addition to tying the central wavelengths of the lines together by their rest wavelengths, we also tie the widths of the oxygen, nitrogen, and sulfur doublets to be the same for each ionic species.

The resulting average gas velocity is 270.8 km s^{-1}. This methodology accurately measures the velocity of an individual H II region to 3.8 km s^{-1}, similar to the uncertainties measured with PPXF. However, there is mild scatter in the velocities of the H II regions of 7.3 km s^{-1}, which contributes to the higher average gas velocity. This result agrees with the H I disk velocity near the PB of ∼268 km s^{-1} (B. K. Rownd et al. 1994) and is in broad agreement with the gas velocities from PPXF in that the gas velocities are larger than the stellar velocities. The mild disagreement with the gas velocities directly from PPXF is likely caused by the large apertures, including any diffuse or extended gas component in the average, blurring the contribution from any individual H II region. Using the gas velocity measured from individual H II regions, the average velocity difference is ∼39 km s^{-1}. As we shall see in the next section, this is consistent within the scatter seen in the spatially resolved velocity maps.

3.2. 2D Velocity Maps

The second method for measuring the radial velocity uses our full IFS coverage to produce 2D velocity maps. This technique complements and extends the aperture method, allowing us to investigate spatial variations in the disk and PB. Other 2D kinematic studies have found that typical spiral galaxies show no abrupt change in the stellar kinematics across a central bulge beyond what is expected in a rotating system (see many of the velocity maps in, e.g., J. Falcón-Barroso et al. 2006; B. Garcìa-Lorenzo et al. 2015; J. Falcón-Barroso et al. 2017; S. Oh et al. 2022). Additionally, there is usually less than a ∼2 km s^{-1} velocity difference between the stellar and gas velocities within the bulge (T. P. K. Martinsson et al. 2013). Therefore, any significant variations in the stellar kinematics alone or between the gas and stellar kinematics in the disk and PB should provide key insights into the nature of the PB.

Again, we use PPXF, as described at the beginning of this section, to extract physical properties from the 2D IFS data. In order to speed up computation time and improve the S/N in each pixel, we spatially bin our data into 3 × 3 pixel (3″ × 3″) bins. We do not split up the stellar continuum and emission line fitting; instead, we opt to fit them simultaneously in one run of PPXF. Note that we still mask the emission lines while fitting the stellar continuum. Finally, we do not bootstrap the model solutions. In its place, we apply regularization, which reduces the noise in the model fit and physical parameters (see Section 3.5 of M. Cappellari 2017 for details).

As with the circular apertures, we extract the stellar and gas kinematics and the mass-weighted ages and metallicities in each binned pixel. We checked the reduced χ^2 values of each model fit, and they were all approximately 1 to 2, indicating that the models are well fit. Similarly, the S/N of each binned pixel was estimated. As expected, given our pointings and light distribution of NGC 5474, the S/N is highest in the PB with a median of ∼35 and decreases further into the disk. Thus, the properties located near or at the PB are likely well determined and have lower uncertainties than those measured in the disk. We subsequently applied an S/N cut on the data and only kept data with an S/N > 5. This reduces the total coverage to the PB and some portions of the disk north and south of the PB, as seen in the following discussion.

Figure 5 shows, from left to right, the stellar velocities, gas velocities, and velocity differences, along with the uncertainties for each quantity. The PB (circled in red) stands out from the disk with $V_* \simeq$ 220–240 km s^{-1}, while clear clumps of H II regions stand out compared to the disk with approximately the same velocities, $V_{\rm gas} \simeq$ 250 km s^{-1}. These combine to make the PB stand out in the velocity difference map in the $|V_{\rm gas} - V_*| \simeq$ 20–40 km s^{-1} range. This result is comparable to the velocity differences measured in the circular apertures in the previous section and strongly supports the idea that the PB is separate from the disk.

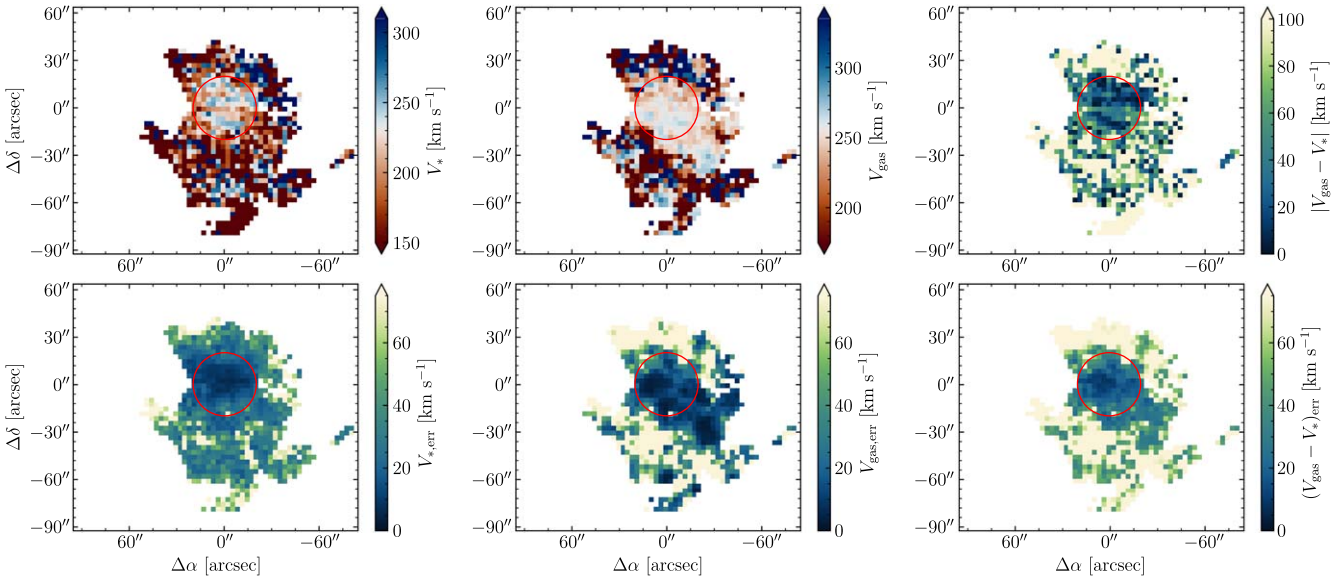

Figure 5. From left to right: the stellar velocities, gas velocities, and velocity differences across NGC 5474. The top row of panels shows the velocities, while the bottom row shows their associated uncertainties. We masked areas of the galaxy where the S/N < 5. The 20″ red circle outlines the position of the PB in each map centered at the origin. North is up and east is to the left.

Given the higher S/N of the data in the PB region, we attempt to search for any signs of rotation in the PB, especially along the disk kinematic axis.[6] The stellar kinematics map in Figure 5 does not appear to show any changing velocities across the PB region. Similar to the technique used in R. Garner et al. (2022), we measure the azimuthal changes in stellar velocities within 10″, 15″, and 20″ of the PB's center in quadrants advanced incrementally by 5°.[7] The results are shown in Figure 6. We have also marked the position angles of the photometric major axis (dashed–dotted line; T. H. Jarrett et al. 2003) and the H I kinematic major axis (dashed; B. K. Rownd et al. 1994).

There does not seem to be any clear preference for rotation around either marked axis nor rotation around any other axis. There is a hint of a signal in the 20″ aperture, but the disk contributes more to this aperture, so this may be a measurement of disk rotation and not PB rotation. Unfortunately, a direct comparison with H I disk rotation curves is not feasible since their resolution precludes measurements at the small radii presented here (B. K. Rownd et al. 1994; D. A. Kornreich et al. 2000). Extrapolating the rotation curve presented by D. A. Kornreich et al. (2000) does suggest rotation signatures $\lesssim$10 km s^{-1}, likely due to the nearly face-on nature of NGC 5474. The lack of measured rotation does suggest that the PB is pressure supported, but higher-resolution data to estimate velocity dispersion more accurately is warranted to make that conclusion.

Figure 7 shows the mass- and light-weighted stellar metallicities and ages across the FOV. We again masked those binned pixels with S/N < 5. We estimate the median mass-weighted metallicity and age of the PB in a 20″ as −0.72 ± 0.23 and 4.1 ± 1.5 Gyr; the median light-weighted metallicity and age of the PB are −0.63 ± 0.22 and 0.8 ± 0.7 Gyr. For comparison, applying the stellar mass of the PB of 5 ± 0.3 × 10^8 $M_\odot$ (G. Bortolini et al. 2024) to the stellar mass–metallicity relation of E. N. Kirby et al. (2013) predicts a stellar abundance of −0.88 ± 0.07, entirely consistent with our estimated abundances. Thus, the PB is likely a low-mass object, consistent with the scaling relations for dwarf galaxies. Unfortunately, the low S/N beyond the bulge precludes a robust measurement of the disk metallicity and age. Higher-resolution spectroscopic data of the stellar

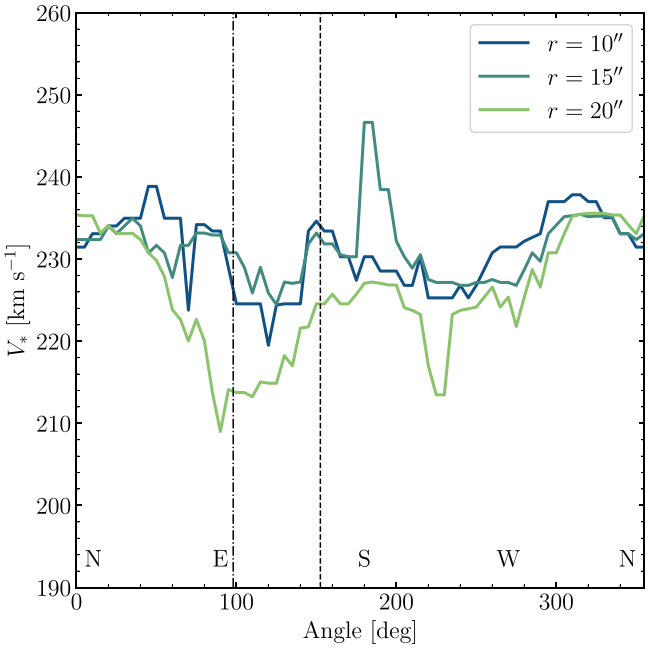

Figure 6. The measured stellar velocities in a quadrant rotated in 5° increments. Angles are measured east from north counterclockwise. Different colors measure the velocities within different aperture sizes indicated in the legend. Characteristic uncertainties for the velocities are 9.0, 10.3, and 12.8 km s^{-1} for the 10″, 15″, and 20″ apertures, respectively. The vertical dashed line is the H I kinematic position angle (158°.5; B. K. Rownd et al. 1994), and the vertical dashed–dotted line is the photometric position angle (98°; T. H. Jarrett et al. 2003).

[6] Due to the low S/N further out in the disk, we cannot make any robust measurement of disk rotation similar to the H I data presented in B. K. Rownd et al. (1994).

[7] We do not use a 5″ aperture due to low number statistics with these binned pixels.

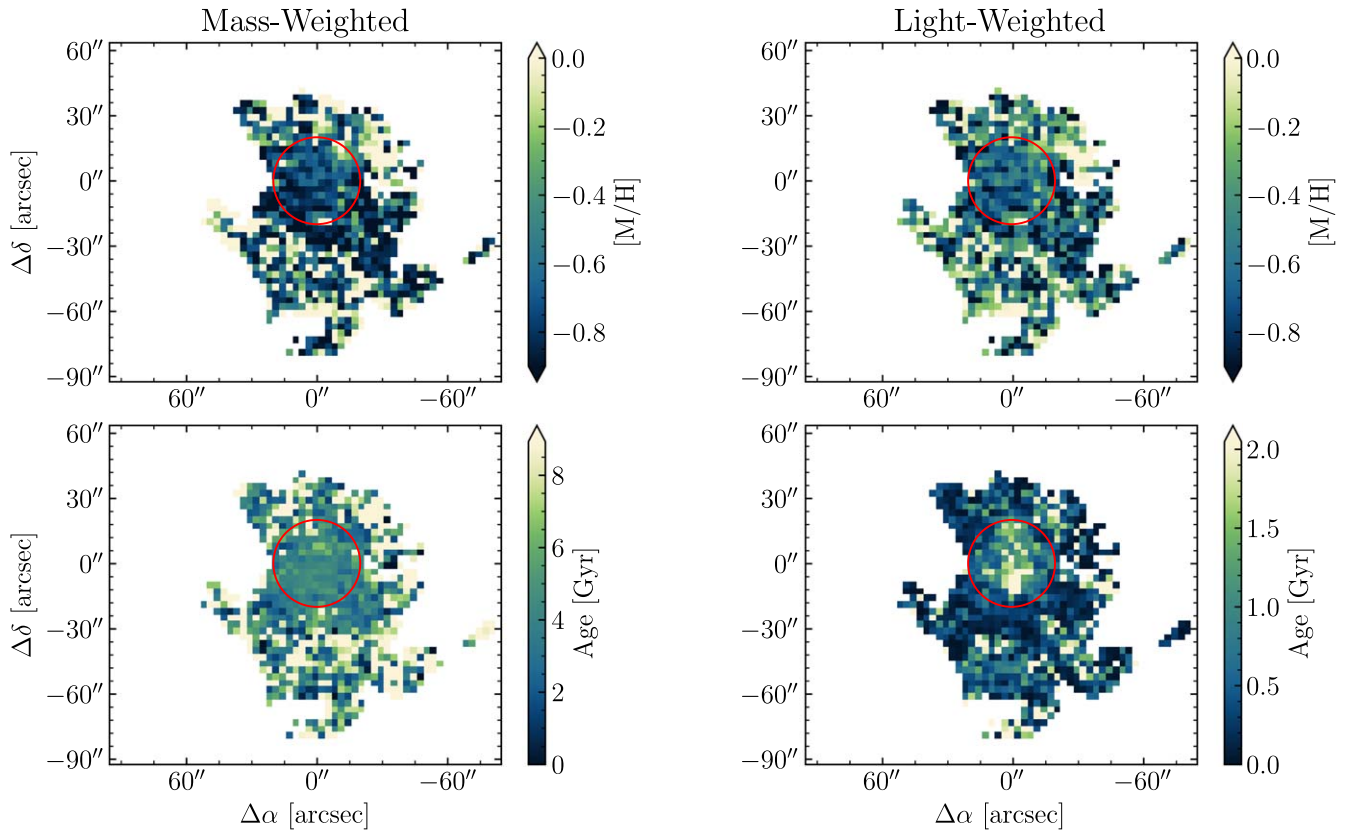

Figure 7. The mass-weighted (left column) and light-weighted (right column) stellar metallicities (top) and ages (bottom) in the FOV. Note the different color bars for the stellar ages. Areas of the data with S/N < 5 were masked. The 20″ red circle outlines the position of PB in each map centered at the origin. North is up and east is to the left.

component of NGC 5474, especially of the disk, are likely needed to make a detailed statement about the metallicities and ages of both components.

4. Summary and Implications

Using data from the PINGS, we have successfully and robustly measured a kinematic offset of $\simeq$24 km s^{-1} between the disk and PB of NGC 5474. This measurement, combined with a wealth of observations (e.g., B. K. Rownd et al. 1994; J. C. Mihos et al. 2013; M. Bellazzini et al. 2020; G. Bortolini et al. 2024), strongly suggests that the PB of NGC 5474 is not a bulge in the same plane as the disk but instead a separate object seen along the line of sight. In the following, we attempt to put the puzzle pieces together, putting the velocity fields, photometry, and simulations in the same context.

Our interpretation that the disk and the PB are separate objects draws on two key observations. The first is the striking velocity offset between the gas and stars in the region of the PB. In a survey of 30 isolated spiral galaxies, T. P. K. Martinsson et al. (2013) compared the ionized gas and stellar velocity offsets. They found a median difference of $V_{\rm gas} - V_{*} = -2.06 \pm 0.20$ km s^{-1} such that the gas velocity is slightly blueshifted compared to the stars, which T. P. K. Martinsson et al. (2013) interpret as due to the near-side expansion of H II regions. The velocity difference in NGC 5474 is an order of magnitude larger than that seen in typical spiral galaxies and in the opposite sense—the gas is redshifted with respect to the stars rather than blueshifted. Furthermore, NGC 5474 is not a strongly star-bursting galaxy (SFR $\simeq$ 0.08 $M_{\odot}$ yr^{-1}; R. C. Kennicutt et al. 2008), lacks an AGN, and the H I disk shows no velocity distortions near the PB (B. K. Rownd et al. 1994). Thus, it is very unlikely that the velocity difference observed is caused by an outflow.

The second observation is the apparent blueshift of the PB compared to the surrounding disk (Figure 5). For isolated spiral galaxies, stellar velocity maps show smooth, regular rotation with no kinematic offset of the bulge (see many of the velocity maps in, e.g., J. Falcón-Barroso et al. 2006; K. Ganda et al. 2006; T. P. K. Martinsson et al. 2013; B. Garcìa-Lorenzo et al. 2015; J. Falcón-Barroso et al. 2017; A. Guérou et al. 2017; S. Oh et al. 2022) unlike what is observed for NGC 5474. Could the velocity offset be a sign that the PB is currently merging with the disk of NGC 5474? Galaxies in the late stages of merging do show distortions to their stellar kinematics (e.g., J. K. Barrera-Ballesteros et al. 2015; J. V. Bloom et al. 2017; R. Nevin et al. 2021; A. Morales-Vargas et al. 2023), but these result in stronger H I kinematic irregularities than is observed for NGC 5474 (B. K. Rownd et al. 1994; D. A. Kornreich et al. 2000). Meanwhile, galaxies in the earliest premerger stages show regular velocity fields with one galaxy being redshifted from the other, such as the optically superimposed galaxy pair VV488 (see Figure B2 in J. K. Barrera-Ballesteros et al. 2015), which is qualitatively similar to NGC 5474. Thus, it is more likely that these two objects, the PB and disk of NGC 5474, are physically separate.

While likely separate, the disk and PB are probably physically associated with each other since the velocity difference between the disk (gas) and PB (stellar) velocities is less than the circular speed of NGC 5474 ($\simeq$44 km s^{-1},

assuming $i = 21°$; B. K. Rownd et al. 1994; D. A. Kornreich et al. 2000). Thus, the PB is likely an external satellite galaxy moving around the disk of NGC 5474 rather than a chance projection of distant objects (R. Pascale et al. 2021). Given the lack of optical tidal features (J. C. Mihos et al. 2013; R. Garner et al. 2021) and distorted velocity fields characteristic of galaxies in the process of merging (e.g., J. K. Barrera-Ballesteros et al. 2015 and references therein), this is probably a weak interaction rather than an actively merging system. Models suggest that NGC 5474 had a previous interaction with M101 ~300 Myr ago (S. T. Linden & J. C. Mihos 2022), and clearly that close passage did not unbind the PB–disk pair. Thus this is likely a somewhat bound pair undergoing a weak interaction.

These findings provide a compelling case that the PB of NGC 5474 is not an intrinsic bulge but rather a distinct satellite galaxy in the early stages of interaction with the disk. This interpretation sheds light on the peculiar dynamics and structure of NGC 5474 and highlights the complex evolutionary pathways that galaxies can undergo. Future work, including higher-resolution spectroscopy of the disk and bulge, as well as simulations and dynamical studies incorporating these two separate bodies into the M101–NGC 5474 interaction (e.g., S. T. Linden & J. C. Mihos 2022), will be essential to confirm the nature of this interaction and explore its role in shaping the observed properties of NGC 5474 and M101. Ultimately, unraveling the nature of this interaction will deepen our understanding of satellite-disk dynamics and the broader processes that drive galaxy evolution in group environments.

Acknowledgments

R.G. would like to thank Grace Olivier and Briana Wirag for helpful comments and insightful discussions. Data here reported were acquired at Centro Astronómico Hispano Alemán (CAHA) at Calar Alto operated jointly by Instituto de Astrofísica de Andalucía (CSIC) and Max Planck Institut für Astronomie (MPG). Centro Astronómico Hispano en Andalucía is now operated by Instituto de Astrofísica de Andalucía and Junta de Andalucía. This research has made use of the NASA/IPAC Extragalactic Database (NED), which is funded by the National Aeronautics and Space Administration and operated by the California Institute of Technology. This research has made use of the Astrophysics Data System, funded by NASA under Cooperative Agreement 80NSSC21M00561.

Facility: CAO:3.5 m (PMAS)

Software: `Astropy` v5.3.4 (Astropy Collaboration et al. 2013, 2018, 2022), `Matplotlib` v3.7.5 (J. D. Hunter 2007), `NumPy` v1.26.4 (C. R. Harris et al. 2020), `SciPy` v1.11.4 (P. Virtanen et al. 2020), `cmcrameri` (F. Crameri 2018), R3D (S. F. Sánchez 2006), E3D (S. F. Sánchez 2004), PINGSOFT (F. F. Rosales-Ortega 2011), PPXF v9.1.1 (M. Cappellari & E. Emsellem 2004; M. Cappellari 2017, 2023), `lineid_plot`[8]

ORCID iDs

Ray Garner III https://orcid.org/0000-0002-9426-7456
J. Christopher Mihos https://orcid.org/0000-0002-7089-8616
F. Fabián Rosales-Ortega https://orcid.org/0000-0002-3642-9146

[8] https://github.com/phn/lineid_plot

References

Astropy Collaboration, Price-Whelan, A. M., Lim, P. L., et al. 2022, ApJ, 935, 167
Astropy Collaboration, Price-Whelan, A. M., Sipőcz, B. M., et al. 2018, AJ, 156, 123
Astropy Collaboration, Robitaille, T. P., Tollerud, E. J., et al. 2013, A&A, 558, A33
Barrera-Ballesteros, J. K., Garcìa-Lorenzo, B., Falcón-Barroso, J., et al. 2015, A&A, 582, A21
Beale, J. S., & Davies, R. D. 1969, Natur, 221, 531
Bellazzini, M., Annibali, F., Tosi, M., et al. 2020, A&A, 634, A124
Bellocchi, E., Arribas, S., & Colina, L. 2012, A&A, 542, A54
Bellocchi, E., Arribas, S., Colina, L., & Miralles-Caballero, D. 2013, A&A, 557, A59
Bloom, J. V., Fogarty, L. M. R., Croom, S. M., et al. 2017, MNRAS, 465, 123
Bortolini, G., Cignoni, M., Sacchi, E., et al. 2024, MNRAS, 527, 5339
Bruzual, G., & Charlot, S. 2003, MNRAS, 344, 1000
Cappellari, M. 2017, MNRAS, 466, 798
Cappellari, M. 2023, MNRAS, 526, 3273
Cappellari, M., & Emsellem, E. 2004, PASP, 116, 138
Crameri, F. 2018, Scientific colour maps v8.0.1, Zenodo, doi:10.5281/zenodo.2649252
Davidson, R., & Flachaire, E. 2008, J. Econom., 146, 162
de Vaucouleurs, G., de Vaucouleurs, A., Corwin, H. G., et al. 1991, Third Reference Catalogue of Bright Galaxies (New York, NY: Springer)
Epinat, B., Amram, P., Marcelin, M., et al. 2008, MNRAS, 388, 500
Falcón-Barroso, J., Bacon, R., Bureau, M., et al. 2006, MNRAS, 369, 529
Falcón-Barroso, J., Lyubenova, M., van de Ven, G., et al. 2017, A&A, 597, A48
Flores, H., Hammer, F., Puech, M., Amram, P., & Balkowski, C. 2006, A&A, 455, 107
Ganda, K., Falcón-Barroso, J., Peletier, R. F., et al. 2006, MNRAS, 367, 46
Garcìa-Lorenzo, B., Márquez, I., Barrera-Ballesteros, J. K., et al. 2015, A&A, 573, A59
Garcìa-Vázquez, J., Henney, W. J., & neda, H. O. C. 2023, MNRAS, 523, 4202
Garner, R., Mihos, J. C., Harding, P., & Garner, C. R. 2024, ApJ, 961, 217
Garner, R., Mihos, J. C., Harding, P., & Watkins, A. E. 2021, ApJ, 915, 57
Garner, R., Mihos, J. C., Harding, P., Watkins, A. E., & McGaugh, S. S. 2022, ApJ, 941, 182
Guérou, A., Krajnović, D., Epinat, B., et al. 2017, A&A, 608, A5
Harris, C. R., Millman, K. J., van der Walt, S. J., et al. 2020, Natur, 585, 357
Ho, L. C., Filippenko, A. V., & Sargent, W. L. 1995, ApJS, 98, 477
Huchtmeier, W. K., & Witzel, A. 1979, A&A, 74, 138
Hunter, J. D. 2007, CSE, 9, 90
Jarrett, T. H., Chester, T., Cutri, R., Schneider, S. E., & Huchra, J. P. 2003, AJ, 125, 525
Kelz, A., Verheijen, M. A. W., Roth, M. M., et al. 2006, PASP, 118, 129
Kennicutt, R. C., Armus, L., Bendo, G., et al. 2003, PASP, 115, 928
Kennicutt, R. C., Lee, J. C., Funes, J. G., Sakai, S., & Akiyama, S. 2008, ApJS, 178, 247
Kirby, E. N., Cohen, J. G., Guhathakurta, P., et al. 2013, ApJ, 779, 102
Kornreich, D. A., Haynes, M. P., & Lovelace, R. V. E. 1998, AJ, 116, 2154
Kornreich, D. A., Haynes, M. P., Lovelace, R. V. E., & van Zee, L. 2000, AJ, 120, 139
Linden, S. T., & Mihos, J. C. 2022, ApJL, 933, L33
Marigo, P., Girardi, L., Bressan, A., et al. 2008, A&A, 482, 883
Mármol-Queraltó, E., Sánchez, S. F., Marino, R. A., et al. 2011, A&A, 534, A8
Martinsson, T. P. K., Verheijen, M. A. W., Westfall, K. B., et al. 2013, A&A, 557, A130
Matheson, T., Joyce, R. R., Allen, L. E., et al. 2012, ApJ, 754, 19
Mihos, J. C., Durrell, P. R., Feldmeier, J. J., Harding, P., & Watkins, A. E. 2018, ApJ, 862, 99
Mihos, J. C., Harding, P., Spengler, C. E., Rudick, C. S., & Feldmeier, J. J. 2013, ApJ, 762, 82
Mihos, J. C., Keating, K. M., Holley-Bockelmann, K., Pisano, D. J., & Kassim, N. E. 2012, ApJ, 761, 186
Morales-Vargas, A., Torres-Papaqui, J. P., Rosales-Ortega, F. F., et al. 2023, MNRAS, 526, 2863
Moustakas, J., Kennicutt, R. C., Tremonti, C. A., et al. 2010, ApJS, 190, 233
Nevin, R., Blecha, L., Comerford, J., et al. 2021, ApJ, 912, 45
Oh, S., Colless, M., D'Eugenio, F., et al. 2022, MNRAS, 512, 1765
Pascale, R., Bellazzini, M., Tosi, M., et al. 2021, MNRAS, 501, 2091
Rosales-Ortega, F. F. 2011, NewA, 16, 220

Rosales-Ortega, F. F., Kennicutt, R. C., Sánchez, S. F., et al. 2010, MNRAS, 405, 735
Roth, M. M., Kelz, A., Fechner, T., et al. 2005, PASP, 117, 620
Rownd, B. K., Dickey, J. M., & Helou, G. 1994, AJ, 108, 1638
Salpeter, E. E. 1955, ApJ, 121, 161
Sánchez, S. F. 2004, AN, 325, 167
Sánchez, S. F. 2006, AN, 327, 850
Sánchez, S. F., Kennicutt, R. C., Gil de Paz, A., et al. 2012, A&A, 538, A8
Sánchez, S. F., Pérez, E., Sánchez-Blázquez, P., et al. 2016, RMxAA, 52, 21
Shapiro, K. L., Genzel, R., Förster Schreiber, N. M., et al. 2008, ApJ, 682, 231
Skrutskie, M. F., Cutri, R. M., Stiening, R., et al. 2006, AJ, 131, 1163
Thilker, D. A., Bianchi, L., Meurer, G., et al. 2007, ApJS, 173, 538
Torres-Flores, S., Amram, P., Mendes de Oliveira, C., et al. 2014, MNRAS, 442, 2188
van der Hulst, J. M., & Huchtmeier, W. K. 1979, A&A, 78, 82
Verheijen, M. A. W., Bershady, M. A., Andersen, D. R., et al. 2004, AN, 325, 151
Virtanen, P., Gommers, R., Oliphant, T. E., et al. 2020, NatMe, 17, 261
Waller, W. H., Bohlin, R. C., Cornett, R. H., et al. 1997, ApJ, 481, 169
Xu, J.-L., Zhang, C.-P., Yu, N., et al. 2021, ApJ, 922, 53